

# The Physics of Protoplanetesimal Dust Agglomerates. IV. Towards a Dynamical Collision Model

C. Güttler and M. Krause

*Institut für Geophysik und extraterrestrische Physik, Technische Universität zu Braunschweig,  
Mendelssohnstr. 3, D-38106 Braunschweig, Germany*

R. J. Geretschauser and R. Speith

*Institut für Astronomie und Astrophysik, Eberhard Karls Universität Tübingen, Auf der Morgenstelle 10,  
D-72076 Tübingen, Germany*

and

J. Blum

*Institut für Geophysik und extraterrestrische Physik, Technische Universität zu Braunschweig,  
Mendelssohnstr. 3, D-38106 Braunschweig, Germany*

## ABSTRACT

Recent years have shown many advances in our knowledge of the collisional evolution of protoplanetary dust. Based on a variety of dust-collision experiments in the laboratory, our view of the growth of dust aggregates in protoplanetary disks is now supported by a deeper understanding of the physics involved in the interaction between dust agglomerates. However, the parameter space, which determines the collisional outcome, is huge and sometimes inaccessible to laboratory experiments. Very large or fluffy dust aggregates and extremely low collision velocities are beyond the boundary of today's laboratories. It is therefore desirable to augment our empirical knowledge of dust-collision physics with a numerical method to treat arbitrary aggregate sizes, porosities and collision velocities. In this article, we implement experimentally-determined material parameters of highly porous dust aggregates into a Smooth Particle Hydrodynamics (SPH) code, in particular an omnidirectional compressive-strength and a tensile-strength relation. We also give a prescription of calibrating the SPH code with compression and low-velocity impact experiments. In the process of calibration, we developed a dynamic compressive-strength relation and estimated a relation for the shear strength. Finally, we defined and performed a series of benchmark tests and found the agreement between experimental results and numerical simulations to be very satisfactory. SPH codes have been used in the past to study collisions at rather high velocities. At the end of this work, we show examples of future applications in the low-velocity regime of collisional evolution.

*Subject headings:* accretion, accretion disks - methods: laboratory, numerical - planetary systems: formation - solar system: formation

## 1. Introduction

### 1.1. Protoplanetary dust growth

The formation of planetesimals, the km-sized solid bodies whose further growth is controlled by

mutual gravitational attraction, is still enigmatic. Collisions among the dust aggregates are controlled by Brownian motion, drift motions with respect to the gas of the protoplanetary disk, and turbulence in the gas (Weidenschilling 1977a; Weidenschilling and Cuzzi 1993). Once in contact, two dust grains experience a mutual van der Waals force (Heim et al. 1999). From the theoretical and experimental standpoints, it is evident that the (sub-)micrometer-sized protoplanetary dust grains initially undergo hit-and-stick collisions, which lead to the formation of fractal aggregates (Weidenschilling and Cuzzi 1993; Blum et al. 2000; Krause and Blum 2004). As the collision energy increases, due to increasing aggregate mass and collision velocity, dust aggregates undergo a restructuring phase, in which they acquire denser structures (Dominik and Tielens 1997; Blum and Wurm 2000; Wada et al. 2007, 2008; Weidling et al. 2009). Laboratory experiments showed that collisions among the dust aggregates result in fragmentation, i.e. in mass loss, if the impact velocities exceed  $\sim 1 \text{ m s}^{-1}$  (Blum and Wurm 2008). Depending on the disk model, this means that the direct collisional growth process ends (at the latest) at aggregate sizes for which this velocity is exceeded. For a minimum-mass solar nebula model (Weidenschilling 1977b; Hayashi et al. 1985), this size is approximately 10 cm.

The further growth is still highly speculative. Wurm et al. (2001) and Blum (2004) proposed the accretion of collisional fragments by aerodynamic and electrostatic effects, respectively. Wurm et al. (2005) and Teiser and Wurm (2009) showed experimentally that a fraction of a dust projectile can stick to a solidified larger dust target even at very large velocities. None of these processes, however, seem to work globally and under all circumstances so that very specific conditions are required for the dust aggregates to grow at high impact velocities. There is clearly a lack of understanding the detailed physics involved in the collisions between macroscopic dust aggregates of arbitrary composition and porosity. Without better knowledge of the collisional physics of these bodies, any attempt to model the formation of planetesimals as an aggregation process will have to fail.

## 1.2. Previous work

In the three previous papers of this series, we described the collisional physics of high-porosity protoplanetary dust aggregates up to the cm-size regime. In paper I (Blum et al. 2006), we introduced a method to experimentally produce monolithic dust aggregates with diameters of 2.5 cm. By choosing either monodisperse spherical monomer particles, quasi-monodisperse irregular particles, or polydisperse irregular grains, we produced dust aggregates with volume filling factors (i.e. packing densities)  $\phi = \rho/\rho_s$  of  $\phi = 0.15$ ,  $\phi = 0.11$ , and  $\phi = 0.07$ , respectively (see Table 1 in paper I for more details about the monomer-particle properties). Here,  $\rho$  and  $\rho_s$  are the aggregate and the monomer density. Static uniaxial compression of these dust samples revealed that the maximum compaction for these high-porosity dust aggregates is  $\phi_{\text{max}} = 0.20 \dots 0.33$ , a value very close to the overall porosity found in comets. The tensile strengths of our dust samples were determined to  $|T| = 200 \dots 6,300 \text{ Pa}$ , depending on the monomer properties and the compaction. Also these values are close to those found for comets. Paper II (Langkowski et al. 2008) concentrated on low-velocity impacts into these high-porosity dust samples. We showed that sticking by penetration is the dominating process for impacts above a threshold velocity of  $\sim 1 \text{ m s}^{-1}$  for projectiles in the mm-size regime and flat dust targets. For shallow penetration, i.e. for impacts below the threshold velocity, the projectiles bounce off, leaving a well-defined crater. It is obvious that the collisions result in the compaction of the target. In paper III (Weidling et al. 2009), we investigated the compaction for high-porosity mm-sized dust aggregates in bouncing collisions. Bouncing collisions among dust aggregates show considerable energy losses (Blum and Münch 1993) so that it was natural to assume some degree of compaction. In paper III, we found that – although a single collision leads only to very localized compaction of the dust aggregate – mm-sized dust aggregates in protoplanetary disks can reach volume filling factors of  $\phi \approx 0.35$  within a few dozen years.

## 1.3. Objectives

All previous experiments (see Sects. 1.1 and 1.2) were limited by the experimentally avail-

able dust-aggregate sizes and morphologies and the achievable collision velocities. In the astrophysical context, the need for numerical simulations of collisions between dust aggregates of arbitrary composition, size and impact velocity arises from the fact that only a limited parameter space can be covered by experiments. The ongoing debate about threshold velocities for sticking, bouncing, compaction, and fragmentation as well as the fragment size distribution requires a thorough investigation of a wide range of collisions, varied over supposedly critical parameters, such as collision velocity, porosity, size, impact parameter, impact angle and shape of the colliding dust aggregates. An extensive parameter study of that kind is not feasible under laboratory conditions for the parameter ranges in question. Therefore, we aim to calibrate a Smooth Particle Hydrodynamics (SPH) code and validate this model thoroughly with a series of independent benchmark tests. Hence, the SPH code gains a deeper reliability and the conducted numerical simulations provide well-grounded insight into the physical behavior of dust aggregates.

## 2. SPH in Dust Collisions

SPH is a meshless Lagrangian particle method originally developed for astrophysical hydrodynamics applications. A detailed description of the original SPH method may, e.g., be found in Monaghan (2005). The SPH code we utilize for the simulations in this work and the underlying porosity model are introduced and described in full depth in Geretshauser et al. (2009). In the 1990s, SPH has been extended to model the elastic and plastic behavior of solids, see e.g. Libersky et al. (1993) and Randles and Libersky (1996). The continuous solid objects are discretized into interacting mass packages called particles, which form a natural frame of reference for any deformation and fragmentation that may occur.

The SPH code solves the equations of continuum mechanics in Lagrangian form, in particular the continuity equation

$$\frac{d\rho}{dt} + \rho \frac{\partial v_\alpha}{\partial x_\alpha} = 0, \quad (1)$$

and the equation of motion

$$\frac{dv_\alpha}{dt} = \frac{1}{\rho} \frac{\partial \sigma_{\alpha\beta}}{\partial x_\beta}. \quad (2)$$

Here, Einstein's summing convention holds throughout and Greek indices denote spatial coordinates. The variables have their usual meanings, i.e.,  $\rho$  denotes the density,  $v$  the velocity, and  $\sigma_{\alpha\beta}$  the stress tensor. The latter is defined according to

$$\sigma_{\alpha\beta} = -p\delta_{\alpha\beta} + S_{\alpha\beta}, \quad (3)$$

consisting of a pressure part with pressure  $p$  and a shear part given by the traceless deviatoric stress tensor  $S_{\alpha\beta}$ .

The deviatoric stress is defined by the constitutive equations. To model elastic behavior according to Hooke's law we adopt the approach by Benz and Asphaug (1994) for the time evolution of the deviatoric stress,

$$\frac{dS_{\alpha\beta}}{dt} = 2\mu \left( \dot{\epsilon}_{\alpha\beta} - \frac{1}{d} \delta_{\alpha\beta} \dot{\epsilon}_{\gamma\gamma} \right) + S_{\alpha\gamma} R_{\gamma\beta} + S_{\beta\gamma} R_{\gamma\alpha}, \quad (4)$$

where  $\mu$  is the shear modulus and  $d$  denotes the dimension. The rotation rate tensor  $R_{\alpha\beta}$  reads

$$R_{\alpha\beta} = \frac{1}{2} \left( \frac{\partial v_\alpha}{\partial x_\beta} - \frac{\partial v_\beta}{\partial x_\alpha} \right) \quad (5)$$

and the strain rate tensor  $\dot{\epsilon}_{\alpha\beta}$  accordingly

$$\dot{\epsilon}_{\alpha\beta} = \frac{1}{2} \left( \frac{\partial v_\alpha}{\partial x_\beta} + \frac{\partial v_\beta}{\partial x_\alpha} \right). \quad (6)$$

This set of equations is closed by a suitable equation of state and describes the elastic behavior of a solid body.

In order to simulate also the plastic behavior of porous bodies, we adopt a modified version of the porosity model by Sirono (2004) (Fig. 1). According to this approach, plasticity is modeled within the equation of state, which is divided into three different regimes. In the first regime, plastic behavior is caused by compression that exceeds a critical limit, the compressive strength  $\Sigma(\rho)$ , while in the second regime, tension exceeds the tensile strength limit  $T(\rho)$ . In between these limits, the third, the elastic regime of the material is described by a special version of the Murnaghan equation of state. Thus, the full equation of state reads

$$p(\rho) = \begin{cases} \Sigma(\rho) & \rho > \rho_c^+ \\ K(\rho'_0)(\rho/\rho'_0 - 1) & \rho_c^- \leq \rho \leq \rho_c^+ \\ T(\rho) & \rho < \rho_c^- \end{cases}. \quad (7)$$

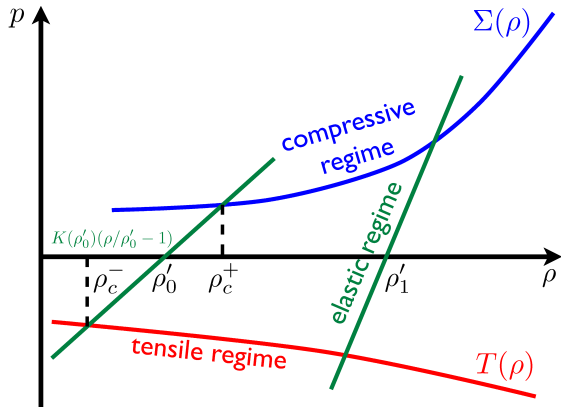


Fig. 1.— The modified Sirono porosity model is divided into the elastic, compressive and tensile regimes. The latter two are reached by exceeding the compressive and tensile strength, respectively, which leads to irreversible plastic deformation.

The quantity  $\rho'_0$  denotes the reference density, which is the density of the material without any external stress.  $\rho_c^+$  and  $\rho_c^-$  are limiting quantities, where the transition between the elastic and plastic regime for compression and tension, respectively, takes place. Once these limits are exceeded, the material leaves the elastic path which represents the path where energy is conserved, and loses internal energy by following the paths of the compressive and tensile strength (Fig. 1).

### 3. Towards an Equation of State for Dust Aggregates

In this laboratory section, we will provide the macroscopic material parameters, which are necessary for the SPH model introduced in section 2. We recapitulate the tensile strength measurements of Blum and Schr apler (2004) and give an interpolation for different volume filling factors. The compressive strength for unidirectional (1D) compression was also measured by Blum and Schr apler (2004), while in this paper we will present measurements on omnidirectional (3D) compression. Moreover, we will introduce a simple impact experiment, which will be used for calibrating the SPH model: A mm-sized glass bead (or a glass bead analog) impacts into a well-defined 2.5 cm dust sample at a collision speed of 0.1 to 1 m s<sup>-1</sup>. The dust sample, consisting of 1.5  $\mu\text{m}$  SiO<sub>2</sub>

monodisperse spheres, was formed by random ballistic deposition (RBD) and has therefore a volume filling factor of  $\phi_0 = 0.15$  (see Blum and Schr apler (2004) and references therein). The deceleration curve, penetration depth and impact duration of the glass bead are measured as well as the compression of the dust beneath the glass bead to compare these results with an impact computed by the SPH model.

#### 3.1. Tensile Strength

In Blum and Schr apler (2004) and paper I, we reported on measurements of the tensile strength of dust samples of various constitutions (i.e. monomer size distribution, morphology, composition, volume filling factor). The best set of data was collected for the dust aggregates consisting of spherical 1.5  $\mu\text{m}$  SiO<sub>2</sub> monomers (see above). For packing densities of  $\phi = 0.15$ ,  $\phi = 0.41$ ,  $\phi = 0.54$  and  $\phi = 0.66$ , we found tensile strengths of  $|T| = 1,000$  Pa,  $|T| = 2,400$  Pa,  $|T| = 3,700$  Pa and  $|T| = 6,300$  Pa, respectively. To a good approximation, these values can be expressed by a relation of the form

$$T(\phi) = - (10^{2.8+1.48\phi}) . \quad (8)$$

This expression will be used throughout this paper for the packing-density-dependence of the tensile strength.

#### 3.2. Static Measurement of Compressive Strength Curves

The compression curve of a given material tells us how the material behaves under an applied pressure  $\Sigma$  in changing its volume filling factor  $\phi$ . If the material can be described by macroscopic parameters, the volume filling factor is representative for the material density and so the development of the compression curve  $\phi(\Sigma)$  (cf. Eq. 7) is essential to establish a collision model and learn about collisions of protoplanetary dust aggregates.

Measurements of the compression curve were already performed by Blum and Schr apler (2004) and in paper I. We will again focus on the dust samples made of 1.5  $\mu\text{m}$  SiO<sub>2</sub> spheres, whose properties are compiled in Table 1 in Blum and Schr apler (2004). In the compression experiments of Blum and Schr apler (2004), a dust sample was fixed between two parallel glass plates,

which were then pushed together with an increasing force. The measurement of the dust mass, dust volume, compression force, and, thus, pressure yield the compression curve  $\phi(\Sigma)$ . The force was applied in one direction, which is therefore called unidirectional compression. The dust sample flattens in the direction of the force but, at the same time, also expands in the other directions. For dust samples made of  $1.5 \mu\text{m}$   $\text{SiO}_2$  spheres, this leads to an equilibrium filling factor of 0.33 for pressures exceeding  $10^5$  Pa. This compression curve is only applicable to protoplanetary dust collisions, if the material compressed in the impact zone creeps sideways as it did in the static experiments. As we will show later by x-ray analysis of the compression next to an impact site, this is not the case.

Consequently, a second way to measure the compressive strength curve is to fix the dust sample at the sides with closed walls. In this case, the pressure cannot be released and acts from all sides, thus omnidirectional compression. We performed experiments in which we cut a cylindrical section from an RBD dust sample with a thin-walled plastic tube of 7 mm diameter. This cylindrical dust sample of approximately 1 cm height was then put into a 7 mm borehole in an aluminum block. Carefully pushing a piston into this borehole leads to an omnidirectional pressure onto the dust sample (see inset in Fig. 2). The setup was put onto a balance and the piston was loaded with weights of increasing mass. This weight force, divided by the piston area, yields the pressure  $\Sigma$ , while the mass and height of the dust sample determine the volume filling factor  $\phi$  (Fig. 2). Due to the fact that the dust sample is not a frictionless fluid, force chains inside the sample might locally reduce the pressure. Thus, the pressure for the idealized compression curve can be slightly lower.

The solid line in Fig. 2 denotes an analytical approximation of the mean filling factor of nine individual experiments as a function of the applied pressure and the gray shaded area is the standard deviation of the measurements. The analytical function is based on a Fermi distribution with logarithmic pressure in the energy term

$$\phi(\Sigma) = \phi_2 - \frac{\phi_2 - \phi_1}{\exp\left(\frac{\lg \Sigma - \lg p_m}{\Delta}\right) + 1} \quad (9)$$

and is only valid for  $\phi \geq \phi_0$ . For pressures below

Table 1: Parameters of the analytical approximation for the two compression curves

	$\phi_1$	$\phi_2$	$p_m$ [kPa]	$\Delta$ [dex]
unidirectional	0.15	0.33	5.6	0.33
omnidirectional	0.12	0.58	13.0	0.58

$\Sigma(\phi_0)$  the dust aggregate behaves elastically. The parameters for the unidirectional and omnidirectional compression curve are given in Table 1. The bottom plot in Fig. 2 gives the deviation between the analytical approximation and the data, which is within  $\phi_{\text{err}} = \pm 0.02$ . Often, the inverse function  $\Sigma(\phi)$  is used (see Eq. 7), which is here

$$\Sigma(\phi) = p_m \cdot \left( \frac{\phi_2 - \phi_1}{\phi_2 - \phi} - 1 \right)^{\Delta \cdot \ln 10} \quad (10)$$

Compared with the unidirectional compression curve (dashed line) of Blum and Schr apler (2004), the filling factor also starts off at the original dust sample filling factor of  $\phi_0 = 0.15$  (cf. Blum and Schr apler 2004), but diverges from the unidirectional curve for pressures  $p \gtrsim 10^3$  Pa.

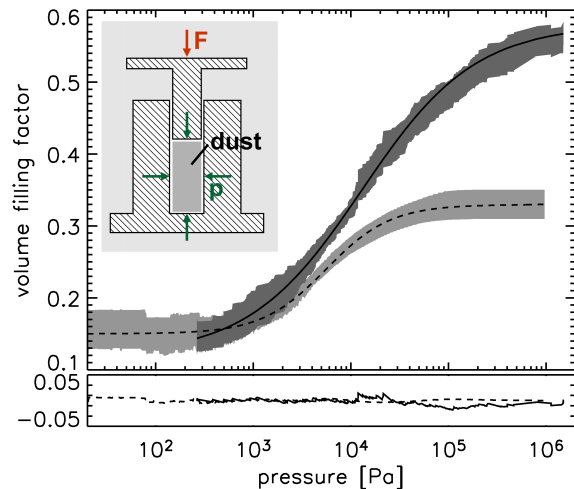


Fig. 2.— The omnidirectional (solid line) and unidirectional (dashed line) static compression curves and the standard deviations of the measurements (gray shaded areas). The upper plot shows the analytical approximations from Eq. 9 and Table 1, while the lower plot gives the deviation between approximation and measurement. The inset describes the setup for the omnidirectional measurement.

For those pressures, the filling factor is systematically higher, meaning on the other hand that the same filling factor is much easier to achieve if the pressure acts from all sides. So far there was no equilibrium filling factor found like in the case of the unidirectional compression experiments. The filling factor still significantly increases for the highest applied pressure of  $10^6$  Pa. However, the analytical approximation indicates an equilibrium for  $\phi_2 = 0.58$ , which is not far from random close packing of monodisperse spheres ( $\phi \simeq 0.64$ , see e.g. Torquato et al. 2000), the maximal possible compression without breaking the dust grains.

The new compression curve is still a static measurement. It is applicable for omnidirectional static pressures like the hydrostatic equilibrium inside planetesimal bodies. It is questionable if this compression curve is valid for dynamic collisions but it is a second attempt to assume that surrounding material, which does not interact in a collision, acts as a confining wall to the active impact volume instead of creeping sideways.

### 3.3. Deceleration Experiments

#### 3.3.1. Experimental Setup

The experimental setup consists of a vacuum chamber (gas pressure  $\sim 0.5$  mbar) in which a projectile is suspended on a thin fiber (Fig. 3) with negligible mass to prevent rotation and lateral velocities. The distance between the suspended projectile and the surface of the dust sample determines the impact velocity  $v_0$ . The projectile consists of an elongated solidified epoxy droplet at the bottom and a cylindrical plastic tube at the top end. After the release of the projectile, it is accelerated by gravity and decelerated once it is in contact with the dust sample. The deceleration within the dust sample is observed by a high-speed camera (Fig. 4). From the deceleration curve of the projectile we can derive fundamental dynamic properties of the target dust aggregate.

The bottom shapes of the projectiles were spherical with diameters of  $R \approx 0.5$  mm and  $R \approx 1.5$  mm and masses of  $m \approx 1$  mg and  $m \approx 30$  mg, respectively (see Table 2). The effective densities of the projectiles of  $\rho = 2,400 \dots 3,100$  kg m $^{-3}$  match those of the astronomically relevant silicates, while the combination of low-density epoxy and plastic tube made sure that the top of the

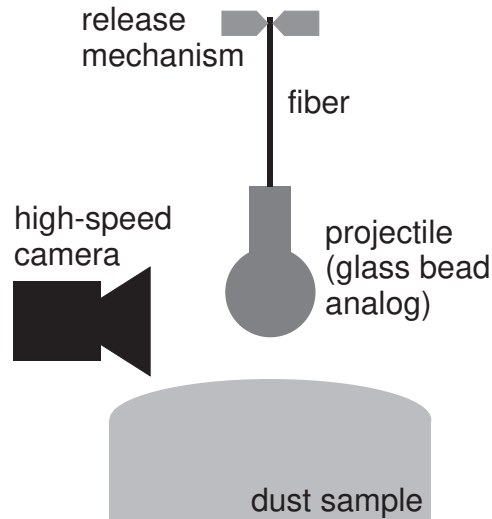


Fig. 3.— Setup for the deceleration measurement: An elongated projectile as a glass bead analog was dropped into the dust sample. Before dropping from a height of 1 to 40 mm, it was suspended on a fiber with negligible mass to avoid rotational motion. A high-speed camera observes the deceleration of the projectile.



Fig. 4.— Image sequence of a decelerated projectile. The time between two images is 1.7 ms.

projectile was always visible to the camera even if the intrusion depth was larger than the projectile diameter. The high-speed camera was operated at a frame rate of 12,000 frames per second with a resolution of  $\sim 30$   $\mu\text{m}$ /pixel and the position of the upper edge of the projectile was measured with sub-pixel accuracy of  $\sim 3$   $\mu\text{m}$ . The first touch of the projectile with the surface of the dust sample marks the time  $t = 0$  and can clearly be determined from the deviation of the trajectory compared to a free falling projectile. After its deepest penetration, the projectile bounces back (by  $\sim 100$   $\mu\text{m}$ ) and oscillates in the vertical direction, which we will not take into account in the further discussion.

Table 2: Experimental results of the deceleration experiments.

experiment number	projectile diameter $2 \cdot R$ [mm]	projectile mass $m$ [mg]	effective projectile density [kg/m <sup>3</sup> ]	impact velocity $v_0$ [m s <sup>-1</sup> ]	penetration depth $D$ [mm]	stopping time $T$ [ms]	standard deviation $\sigma$ for polynomial [ $\mu\text{m}$ ]	standard deviation $\sigma$ for sine [ $\mu\text{m}$ ]
1	2.73	25.7	2412	0.89	3.16	5.92	2.43	21.48
2	2.94	32.0	2404	0.85	3.08	5.93	2.99	22.64
3	2.77	26.4	2372	0.73	2.70	6.09	1.87	17.29
4	2.94	32.0	2404	0.17	0.70	6.18	4.63	10.78
5	2.94	32.0	2404	0.16	0.75	7.13	2.84	7.69
6	2.94	32.0	2404	0.20	0.80	5.92	2.96	8.95
7	2.94	32.0	2404	0.32	1.31	6.47	1.62	2.53
8	2.77	27.6	2480	0.50	2.03	6.38	1.82	3.57
9	2.77	26.4	2372	0.37	1.33	5.71	3.65	6.26
10	0.99	1.5	2854	0.67	1.06	3.09	3.48	27.77
11	0.99	1.5	2854	0.76	1.15	2.94	1.41	23.24
12	0.99	1.5	2854	0.79	1.47	3.12	14.29	5.62
13	0.85	1.0	3109	0.19	0.32	2.46	1.94	3.79
14	0.85	1.0	3109	0.35	0.83	3.28	2.60	11.15
15	0.85	1.0	3109	0.36	0.72	3.11	2.71	3.73

### 3.3.2. Experimental Results

We performed 15 impacts of our projectiles into the porous dust samples, which are compiled in Table 2. The time-resolved deceleration data  $h(t)$  were cleaned from gravitational influence by adding  $\frac{1}{2}gt^2$  to the negative intrusions so that the gravity-independent deepest penetration depth  $D$  and stopping time  $T$  could be determined. The intrusion curves were normalized in space and time through  $h'(t') = h(t)/D$  and  $t' = t/T$  so that  $h'(t' = 0) = 0$  (first contact) and  $h'(t' = 1) = -1$  (deepest intrusion), and can then be well represented by a sine function

$$h'(t') = -\sin\left(t' \cdot \frac{\pi}{2}\right). \quad (11)$$

Alternatively, a fourth order polynomial with only one free parameter was used for fitting the data, where the mean standard deviation between the fit and the  $N$  data points  $\sigma = \sqrt{\frac{1}{N} \sum_{i=1}^N (h'(t'_i) - h'_i)^2}$  amounts to only 2 – 4  $\mu\text{m}$  in absolute units (cf. Table 2). Although the standard deviation for the sine function is rather of the order of 10  $\mu\text{m}$ , we take the sine function because it has no free parameter and the standard deviation is still less than the pixel size of 30  $\mu\text{m}$ . In few experiments, the 1 mm projectiles canted over before coming to rest. In these cases, the data was used as long as reliable and the remaining deceleration curve and, thus, the penetration depth was extrapolated.

Figure 5 shows all measured deceleration curves in absolute units. Different intrusion depths and stopping times can clearly be distinguished in this

plot. The intrusion depths increase with increasing impact velocities (i.e. with the absolute values of the initial slopes of the curves), while the stopping times are rather constant for one projectile size ( $T \sim 6$  ms for 3 mm projectiles [nos. 1-9 in Fig. 5] and  $T \sim 3$  ms for 1 mm projectiles [nos. 10-15 in Fig. 5]) and, thus, independent from the impact velocity  $v_0$ . A  $\chi^2$  test yielded the best-fitting power-law relation between the penetration depth, impact velocity and mass of the form

$$D = \gamma_D \cdot m^{\alpha_D} \cdot v_0^{\beta_D}, \quad (12)$$

with  $\alpha_D = 0.23 \pm 0.13$ ,  $\beta_D = 0.89 \pm 0.34$ , and  $\gamma_D = (3.86 \pm 0.11) \cdot 10^{-2} \text{ kg}^{-0.23} \text{ m}^{0.11} \text{ s}^{-0.89}$  (Fig. 6). The respective errors denote the  $1\sigma$  uncertainties. A more intuitive relation would be  $D \propto mv_0 A^{-1}$ ,

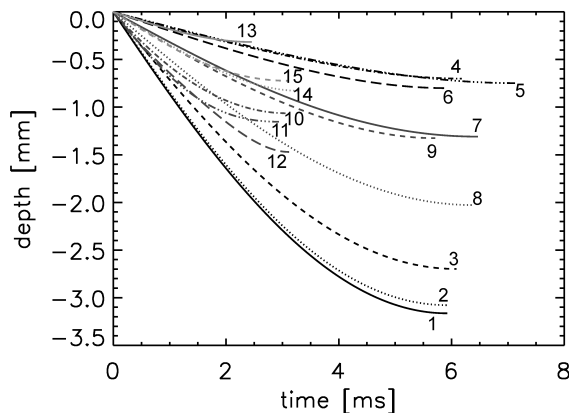


Fig. 5.— Fitted deceleration curves in absolute units. The experiment numbers at the deceleration curves confer to those in Table 2.

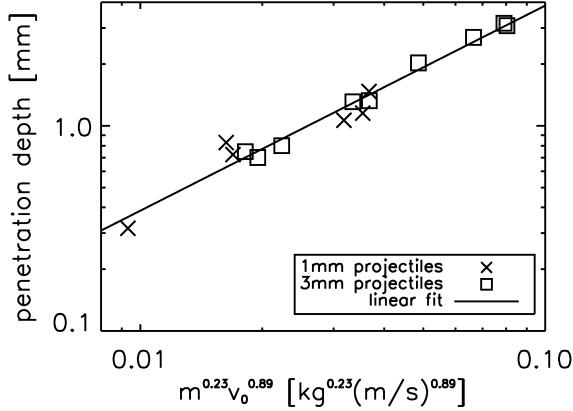


Fig. 6.— The best relation for the penetration depths from a  $\chi^2$  test yields a dependence of  $D \propto m^{0.23} v_0^{0.89}$ . The intuitive relation  $D \propto m v A^{-1}$  is possible within the uncertainties.

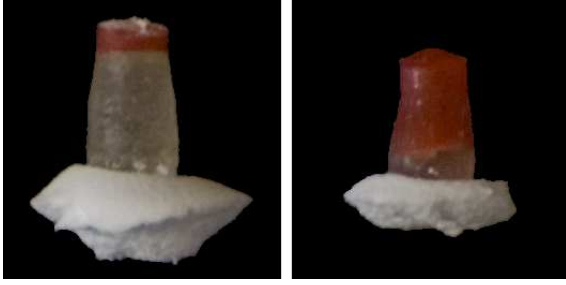


Fig. 7.— Dust sticks to the projectiles after pulling them out of the dust sample. This is an indication of compacted material under the projectile as will be confirmed in Sect. 3.4.

with  $A = \pi R^2$  being the cross section of the projectile. This relation has a clear physical meaning as the penetration depth is determined by the quotient of the momentum  $m v_0$  as driving force and the cross sectional area  $A$  as resistive parameter. With  $\alpha_D = \frac{1}{3}$  and  $\beta_D = 1$  being possible within the uncertainties, the linear relation  $D \propto m v_0 A^{-1} \propto \rho_p^{1/3} R v_0$  is also possible. However, constraining the exponent  $\delta_D$  as  $D \propto \rho_p^{\delta_D}$  in Eq. 12 was unfortunately not feasible due to the too small variations in the effective projectile density  $\rho_p$  (cf. Table 2).

For the stopping time, we found

$$T = \gamma_T \cdot m^{\alpha_T} \cdot v_0^{\beta_T} \quad (13)$$

with  $\alpha_T = 0.23 \pm 0.08$ ,  $\beta_T = 0.01 \pm 0.23$ , and  $\gamma_T = (6.77 \pm 0.20) \cdot 10^{-2} \text{ kg}^{-0.23} \text{ m}^{-0.01} \text{ s}^{1.01}$  was

found for the stopping time.

After pulling the projectiles out of the dust sample, dust stuck to the surface with which it had been in contact before (Fig. 7). With the preliminary assumption that this is compacted dust and the layer where it broke off is the transition from compacted to non-compacted dust (transition in tensile-strength), this gives an indication for the compressed volume which will be analyzed in detail in the forthcoming section.

### 3.4. Dynamic Compression Experiments

#### 3.4.1. Experimental Setup

In order to investigate in more detail the compression behavior of the dust aggregates by collisions, we performed impact experiments with subsequent x-ray micro-tomography measurements to analyze the degree of compaction.

Under vacuum conditions we dropped a single glass spherule with a diameter of  $\sim 1$  mm from a given height of  $\sim 75$  mm into an RBD dust sample within a plastic tube with 7 mm diameter. To ensure the sphere to preferably hit the center of the dust sample within the narrow plastic tube, the released projectile was guided by falling through a tube. Due to friction and collisions with the tube's walls the impact velocity of  $(0.8 \pm 0.1) \text{ m s}^{-1}$ , that was independently measured by high-speed imaging in 10 drops, is much lower than expected from free fall. However, the velocity in the specific experiment was not measured and can well be in the lower range of the error. From comparison of

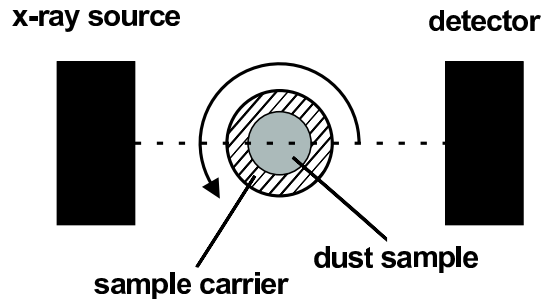


Fig. 8.— Setup of the x-ray micro-CT measurement: the sample is rotated between an x-ray source and a detector. A 3D density reconstruction can be computed from the transmission images.



the observed penetration depth (see Fig. 9 in Sect. 3.4.2) with the results in Fig. 6 we expect a velocity of  $v = 0.65 \text{ m s}^{-1}$ , which we will use for the further study.

For analyzing the density distribution of the dust sample cutout with the embedded glass sphere, the dust sample was scanned by an x-ray micro-computer-tomograph (Micro-CT SkyScan 1074) at the University of Osnabrück. The dust sample was positioned on top of a rotatable sample carrier between the x-ray source and the detector (CCD camera) (Fig. 8). While rotating stepwise around by  $360^\circ$ , 400 transmission images were captured. Based on this data set, a 3-dimensional density reconstruction was calculated by the SkyScan Cone-Beam Reconstruction Software provided with the x-ray micro-CT instrument.

### 3.4.2. Experimental Results

In the following we present the results of two impact experiments. Further experiments with differently sized spheres and different impact velocities are intended. To visualize the spatial density distribution of the observed dust sample with the impacted glass sphere, the 3-dimensional reconstruction data was cylinder-symmetrically averaged with the vertical axis aligned with the sphere center. Figure 9 displays the mean volume filling factor as a function of height and radius, whereas the data is mirrored with respect to the vertical center line of the diagram. The color gradient from yellow to light blue underneath the impacted sphere (red color: saturated density values of the considerably denser glass spherule) clearly shows the densification of the porous dust sample with an initial volume filling factor of  $\phi_0 \approx 0.15$ . The compressed area, emphasized by overplotted contour-lines, is located almost cylindrically shaped beneath the sphere and extends only slightly to the lateral borders of the sphere. Thus, the assumption of an omnidirectional compression curve, made in Sect. 3.2, seems to be justified.

Analysis of the distribution of occurring volume filling factors related to their fraction of volume within an uncompressed dust sample provides a Gaussian-shaped distribution with a mean value of  $\phi \approx 0.15$  (Fig. 10). Figure 11 (top) shows the volume fraction (normalized by the sphere volume) of volume filling factors, which we determined only

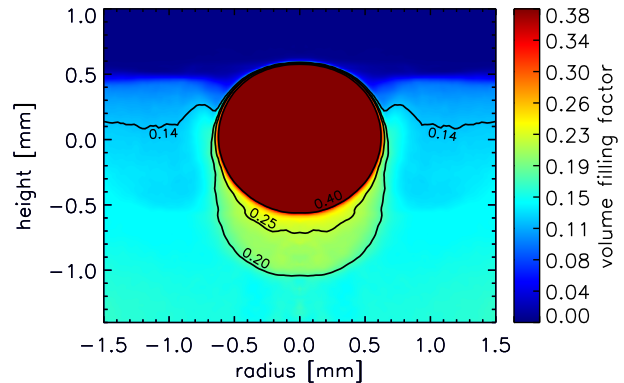


Fig. 9.— Spatial averaged volume filling factors mirrored at the vertical center line. The volume under the sphere is compacted to a volume filling factor  $> 0.2$  (yellow), while the surrounding material is nearly unaffected (light blue).

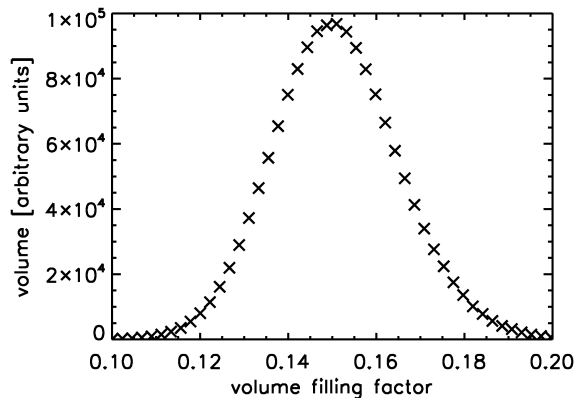


Fig. 10.— Distribution of volume filling factors for an uncompressed dust sample, which follows a Gaussian distribution with a mean value of  $\phi \approx 0.15$ .

regarding the compacted volume underneath the impacted sphere for the two impact experiments. In both curves the most prominent volume filling factor is around  $\phi = 0.23$ , indicated by the dashed and dotted lines. The decreasing left flank of the curves corresponds to the transition region between compressed and uncompressed dust material (see right curve flank of Fig. 10). The same data plotted in a cumulative way (Fig. 11, bottom), represent the amount of compacted volume in units of the sphere volume that complies with a volume filling factor greater than a certain value. According to the volume filling factor values at

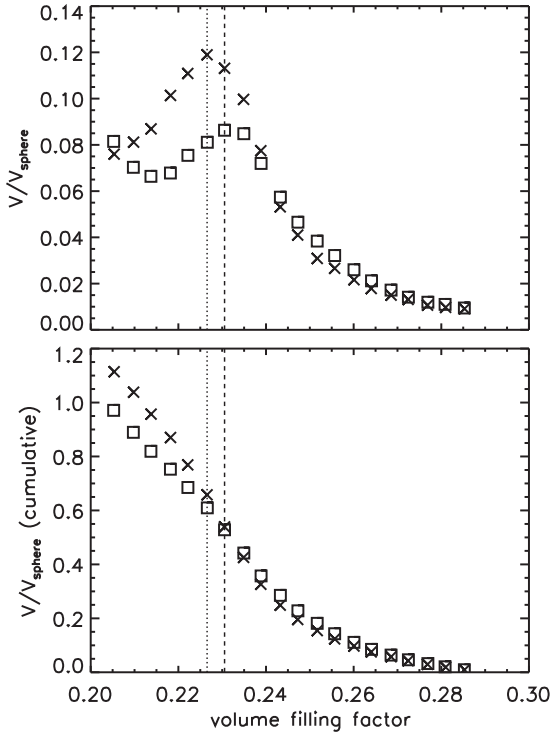


Fig. 11.— **Top:** Distribution of volume filling factors only for the compressed area underneath the impacted sphere for two experiments. The dashed and dotted lines mark the most occurring volume filling factors for each curve, lying at  $\phi \approx 0.23$ . **Bottom:** Normalized volume fraction of compacted area corresponding to a volume filling factor  $> \phi$ .

the boundary to the uncompressed dust, given by the minima of the left side of the curves in Fig. 11 (top), we can conclude from the cumulative curves (Fig. 11, bottom) that the compressed volume due to an impacting sphere of 1 mm size into a high-porosity dust sample ( $\phi \approx 0.15$ ) fills the volume of  $\sim 0.8$ -1.2 sphere volumes.

### 3.5. Requirements of a Dynamic Compressive Strength Curve

As seen in the previous sections, we have abundant indirect information about the compression behavior of loose dust samples. However, the basic question how the dynamic compressive strength curve,  $\phi(\Sigma)$ , looks, remains unanswered. We ap-

proach this problem the following way: (1) For low compressions,  $\Sigma \rightarrow 0$ , the volume filling factor is given by the initial properties of the material, i.e.  $\phi \rightarrow \phi_1$  (see Table 1). (2) The maximum compression for  $\Sigma \rightarrow \infty$  is given by the value  $\phi_2$  in Table 1 for the omnidirectional case, because the XRT analysis shows no material creeping sideways as was the case for the unidirectional flow (see Blum and Schr apler 2004). (3) With these two limits in mind, we apply Eq. 9 as an approximation to the functionality of the dynamic compressive strength, which leaves us with the two free parameters  $\Delta$  and  $p_m$ . The maximum slope of the compression at  $\Sigma = p_m$  is given by  $d\phi/d \lg \Sigma = (\phi_2 - \phi_1)/\Delta$ . For the unidirectional and omnidirectional static curves, we get slope values of 0.55 and 0.79, respectively (see Table 1). These are in fact not so different so that we adopt for the dynamic case the slope of the omnidirectional compression. Thus, we assume  $\Delta = 0.58$  dex for the dynamic case. A refined study that takes both,  $\Delta$  and  $p_m$ , as free parameters will be conducted in Geretshauser et al. (2009), but in this paper we only vary  $p_m$ .

## 4. Calibrating the SPH code

The laboratory experiments in the previous section provided the static omnidirectional compressive strength  $\Sigma$  and the tensile strength relation  $T$  as most important ingredients for the Sirono porosity model implemented in the SPH code by Geretshauser et al. (2009). However, as it was already pointed out in the laboratory section, the compressive strength relation has to be considered dynamically. The only free parameter  $p_m$  (see Sect. 3.5) cannot be determined by experiments. Hence it has to be constrained by a numerical parameter study. We will use the stopping time of the impacting glass bead as reference for this parameter.

In addition, a relation for the shear strength is also very hard to measure in the laboratory. Therefore, we suggest three simple relations depending on the dynamic compressive strength and tensile strength relations and use the qualitative comparison of the filling factor profile under the glass bead after impact to constrain this unknown quantity.

Finally, we utilize the remaining experimentally

measured independent features of the experiments described in the laboratory section to validate our calibration.

#### 4.1. Benchmark test - setup

The given experimental setup (see Sect. 3.4) was modeled with high resolution in two dimensions. Initially, the SPH particles were put on a triangular grid. All simulations were performed with the influence of gravity taken into account.

The projectile was modelled with a circle of 1.1 mm in diameter consisting of 1519 SPH particles. Its material properties were simulated using the Murnaghan equation of state

$$p = \left( \frac{K_0}{n} \right) \left[ \left( \frac{\rho}{\rho_0} \right)^n - 1 \right] \quad (14)$$

with  $\rho_0 = 2540 \text{ kg m}^{-3}$  (total 2D mass per unit length  $m_{2D} = 2.4 \cdot 10^{-3} \text{ kg m}^{-1}$ ),  $K_0 = 5.0 \cdot 10^9 \text{ Pa}$  and  $n = 4$ . The density has been chosen such that it matches the experimental specifications. The other material parameters are similar to those of sandstone. They can be found together with the Murnaghan equation of state in Melosh (1989). The exact choice of the bulk modulus  $K_0$  and the Murnaghan exponent  $n$  does not have significant effects. The glass bead was treated as fully elastic. The impact velocity was  $0.65 \text{ m s}^{-1}$ .

The dust sample was modelled as a  $8 \times 5 \text{ mm}^2$  rectangle with 64421 SPH particles. About 0.15 mm at the bottom and 0.56 mm at each side of the rectangle were used as reflecting boundary by setting their acceleration to zero at each time step. The porous material was simulated by using the modified version of the Sirono model presented in Sect. 2. The initial density was expressed via the filling factor  $\phi = \rho/\rho_0$  with  $\phi = 0.15$  and  $\rho_0 = 2000 \text{ kg m}^{-3}$ . For the tensile strength we used the semianalytical relation, derived in Sect. 3.1 (Eq. 8) that matches the findings of Blum and Schr apler (2004) and paper I. The bulk modulus was modeled by a power law

$$K(\rho) = K_0 \left( \frac{\rho}{\rho_i} \right)^4 \quad (15)$$

with  $K_0 = 300 \text{ kPa}$  and the initial density of the dust aggregate  $\rho_i = 300 \text{ kg m}^{-3}$ . The bulk modulus  $K_0 = \rho_i c^2$  for uncompressed material was determined by the measurement of the sound speed,

which is  $c = 30 \text{ m s}^{-1}$  (Blum and Wurm 2008; Paszun and Dominik 2008).

For the compressive strength, several different relations were tested. At first we adopted the relation from the uniaxial experiments by Blum and Schr apler (2004). Secondly we used the omnidirectional compression curve presented in this paper. After it turned out that a modified relation for the dynamical compressive strength curve had to be considered, the omnidirectional compression curve (Eq. 10) was shifted towards lower pressure regimes using the free parameter  $p_m$  (see Sect. 3.5).

Since no experimental data was available for the shear strength  $Y$ , parameter studies were carried out with three different relations  $Y(|T|, \Sigma)$ :  $Y = |T|$ ,  $Y = \Sigma$  and, following Sirono (2004),  $Y = \sqrt{\Sigma|T|}$ , which represents the geometric mean of both quantities.

Due to reasons of stability, the two materials in contact (solid projectile, dusty target) have to be separated by artificial viscosity. We use the approach by Monaghan and Gingold (1983) and apply an  $\alpha$ -viscosity of 1.0 to all particles of the sphere and all particles interacting with the sphere. All other dust-sample particles were simulated without artificial viscosity following Sirono (2004). All details regarding the SPH code can be found in Geretshauser et al. (2009).

#### 4.2. Calibration procedure

With the aim of reproducing the experimental results presented in the laboratory section, an SPH simulation using the omnidirectional compressive strength curve (ODC) was conducted. In the resulting pressure regime the ODC relation and the relation from Blum and Schr apler (2004) are almost identical. Therefore they can be treated as one case.

The impact velocity of the 1.1 mm glass bead was  $0.65 \text{ m s}^{-1}$  and we will compare the results of the simulation with the vertical density profile along a line through the center of the sphere perpendicular to the bottom of the dust sample, which was measured with x-ray micro-tomography as described in Sect. 3.4. Figure 12 shows the results for three different shear strength models, which are compared to two density profiles as measured in the experiments (lines with blue and green

crosses). The initial surface of the dust sample is at 0 mm.

For the original ODC relation ( $p_m = 13$  kPa), the simulations for all shear strength models resulted in a much too shallow intrusion depth and an insufficient maximum filling factor underneath the sphere. These findings indicated, that the compressive strength curve had to be modified in order to reproduce the experimental data. Therefore, we performed a parameter study varying the parameter  $p_m$ , i.e. shifting the compressive strength curve to lower pressures for the different shear strength models. For the complete study see Geretshauser et al. (2009). Independent experiments (paper III) also support a lower  $p_m$  which can quantitatively explain the amount compression in bouncing collisions.

A significant increase of the intrusion depth was only observed in case of  $Y = \sqrt{\Sigma|T|}$  and  $Y = \Sigma$  (see Fig. 12, top and center). In case of  $Y = |T|$  the intrusion depth hardly changed with decreasing  $p_m$  (Fig. 12, bottom). Since the shear strength remained constant and changing  $p_m$  did not have a significant effect, it can be concluded that shearing plays an important role during the intrusion.

Compared to the other cases, the shear strength reaches its highest values in the  $Y = |T|$  case. Hence, the material can hardly be pushed away due to shear and has to be compressed. Therefore, the highest filling factors can be found in this case (see Fig. 12, bottom). The  $Y = \Sigma$  model yields the lowest shear strength values. Hence, material is mostly sheared aside, less material is compressed and therefore this model leads to filling factors below the reference data (see Fig. 12, center).

Figure 13 shows intrusion depth over stopping time regarding the shear strength models  $Y = \Sigma$  and  $Y = \sqrt{\Sigma|T|}$  for all  $p_m$ . Since  $Y = |T|$  did only yield insufficient intrusion depths, this model was omitted here. A good time/depth match was achieved for  $p_m = 3.9$  kPa using  $Y = \Sigma$  and for  $p_m = 1.3$  kPa using  $Y = \sqrt{\Sigma|T|}$ . However, the  $Y = \Sigma$  model cannot reproduce the high values in the vertical filling factor profile (Fig. 12, center) whereas the  $Y = \sqrt{\Sigma|T|}$  model yields an almost perfect match (Fig. 12, top). Therefore, the latter with  $p_m = 1.3$  kPa gives a good match in Fig. 12 (top) as well as in Fig. 13 and is therefore used for further simulations. A more detailed study on the determination on the  $p_m$  value can be found

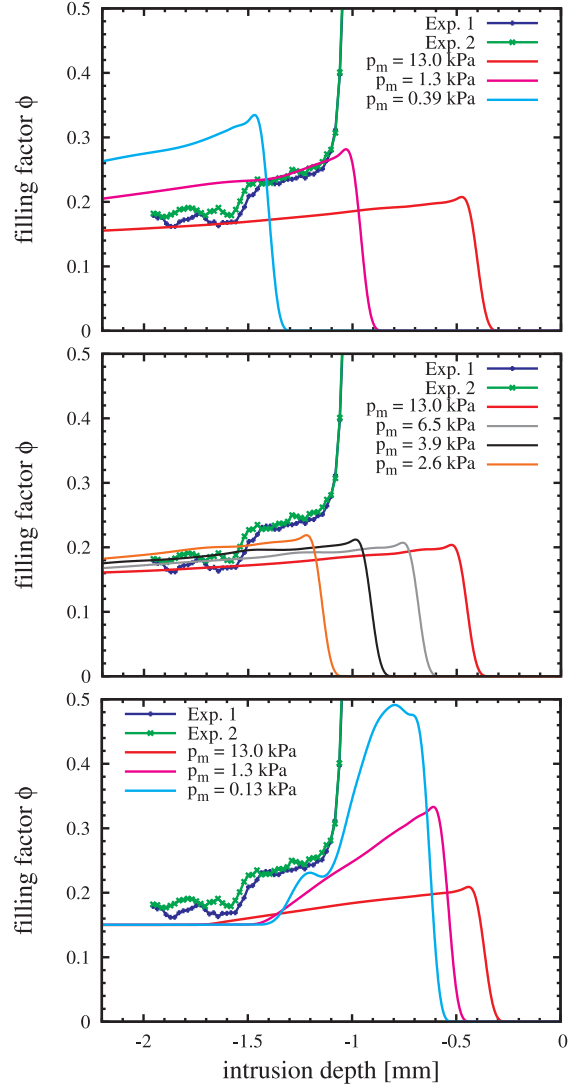


Fig. 12.— The filling factor measured along a line through the center of the sphere, perpendicular to the bottom of the dust sample (lines with blue and green crosses). The initial surface of the dust sample is situated at 0 mm and the steep slope at the right end of the experimental curves marks the transition from the dust sample to the glass sphere. The other curves are numerical simulations, varying the shear strength model and the material softness  $p_m$ . The shear strength relation was **(top)**  $Y = \sqrt{\Sigma|T|}$ , **(center)**  $Y = \Sigma$ , and **(bottom)**  $Y = |T|$ .

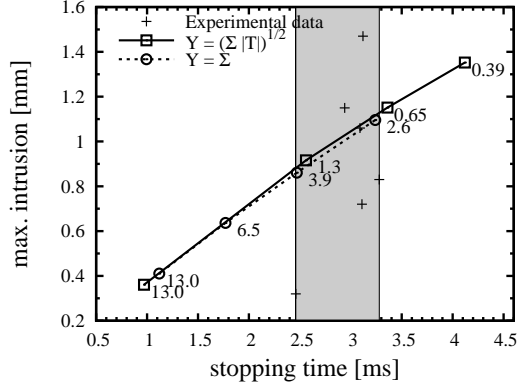


Fig. 13.— Stopping time - intrusion diagram. Experimental data for spheres of 1 mm radius. Labels indicate the  $p_m$  values (in kPa) for the modification of the compressive strength curve. For the  $Y = \Sigma$  model the best match in stopping time and intrusion depth is found for  $p_m = 3.9$  kPa. For the  $Y = \sqrt{\Sigma|T|}$  model the best approximation is given for  $p_m = 1.3$  kPa.

in Geretschauser et al. (2009).

Hereby, we have determined parameters for all previously unknown material relations and thus have calibrated the SPH model with respect to the presented experiments. The resulting strength curves of compression (Eq. 10,  $p_m = 1.3$  kPa), tension (Eq. 8) and shear ( $Y = \sqrt{\Sigma|T|}$ ) are illustrated in Fig. 14.

However, the fact that the filling factor does not rapidly drop to  $\sim 0.15$  at a depth of 1.5 mm requires further investigation.

### 4.3. Reproducing Experimental Features

Since intrusion time and depth as well as the filling factor profile underneath the sphere have been used to determine  $p_m$  and the correct shear strength model, further features have to be reproduced in order to validate the calibration.

One of these features is the cumulated volume over filling factor relation (Fig. 15). While the filling factor profile only displays a cut through the compressed volume, this curve represents the total compressed volume with its filling factors. Both curves are not fully, but mostly independent from each other. The chosen model and  $p_m$  value yield an almost perfect match for filling factors  $> 0.22$ . The deviation for lower filling factors is due to the

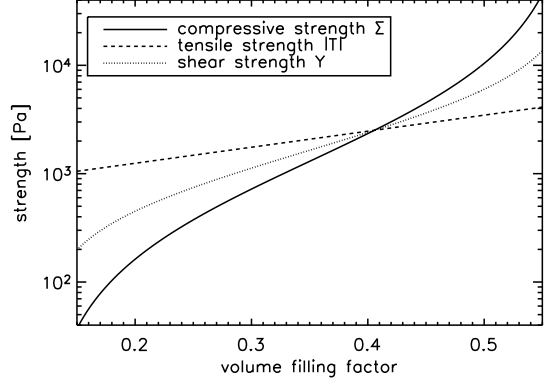


Fig. 14.— Compressive strength curve  $\Sigma(\phi)$  (Eq. 10) for  $p_m = 1.3$  kPa, tensile strength  $|T|$  (Eq. 8), and shear strength  $Y = \sqrt{\Sigma \cdot |T|}$ .

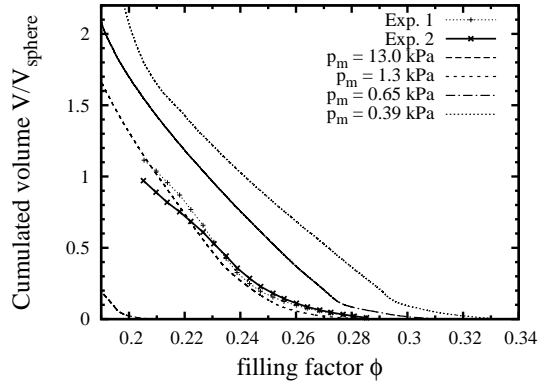


Fig. 15.— Cumulated volume over filling factor. While  $p_m = 13$  kPa, i.e. the unmodified ODC relation, and  $p_m = 0.39$  kPa as well as  $p_m = 0.65$  kPa yield too small and too high compression values, respectively,  $p_m = 1.3$  kPa matches very well for  $\phi \gtrsim 0.22$ . The experimental data are identical to those shown in Fig. 11 (bottom)

larger amount of compressed volume. This effect was already seen in the filling factor profile and is also very prominent in the comparison of the spatially density distribution plots (compare Figs. 9 and 16).

Another feature to be reproduced is the relation  $D \propto mvA^{-1}$  found in a similar way in the drop experiments (cf. Fig. 6). We performed a series of 2D simulations with spheres of 1 mm and 3 mm diameter and evaluated the maximum intrusion depth with respect to the impact velocity  $v$ .

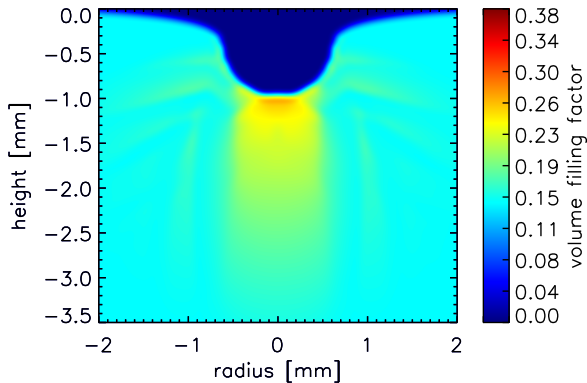


Fig. 16.— Spatially distributed compression as calculated in the SPH simulation with  $Y = \sqrt{\Sigma \cdot |T|}$  and  $p_m = 1.3$  kPa; same color scale as Fig. 9; the projectile is not plotted. Although the filling factor of compressed material is comparable to the one in the experiments, the compressed volume reaches significantly deeper.

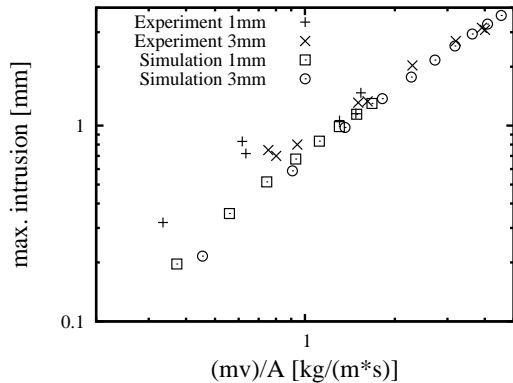


Fig. 17.— In the momentum-intrusion relation, the agreement between simulation and experimental results is very good for values of  $mvA^{-1} \gtrsim 1$   $\text{kg m}^{-1} \text{s}^{-1}$ .

The latter was varied from  $0.1 \text{ m s}^{-1}$  to  $1.0 \text{ m s}^{-1}$  in steps of  $0.1 \text{ m s}^{-1}$ .

2D simulation and experiment cannot be compared directly due to the different geometry (the 2D setup represents a cut through an infinitely long cylinder). The advantage of using the quantity  $mvA^{-1}$  instead of the more accurate Eq. 12 is given by the fact that the former can be “con-

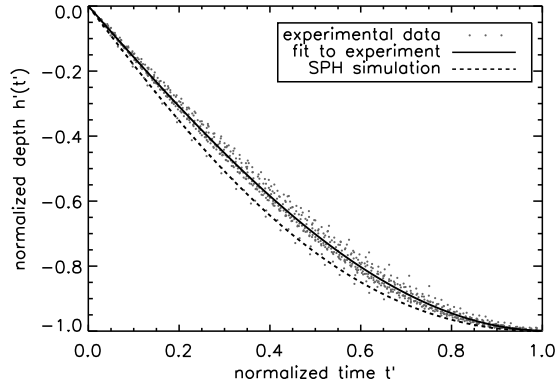


Fig. 18.— Normalized deceleration curve compared to the results. The deceleration curve in the SPH simulation is slightly lower than the experimentally observed sine curve, but well within the errors. This effect will be analyzed in future work. However, the range of experimental data encompasses the simulation results.

verted” into 2D by the following correction:

$$\frac{m_{3D}v}{A_{3D}} = \frac{\frac{4}{3}\pi r^3 \rho \cdot v}{\pi r^2} = \frac{8}{3\pi} \frac{\pi r^2 \rho \cdot v}{2r} = \frac{8}{3\pi} \frac{m_{2D}v}{A_{2D}} \quad (16)$$

In comparison with the experimental results, the data from the simulation matches very well for  $mvA^{-1} > 1.0 \text{ kg m}^{-1} \text{ s}^{-1}$  (Fig. 17). For smaller values the simulation yields a shallower intrusion than the reference experiments, which, however, also show significant scattering in this range.

Comparing the simulated and experimentally acquired normalized deceleration curves (Fig. 18), the simulated data slightly deviate from the experimental mean but remain within standard deviation limits. The deviation could arise from the geometric difference of the 2D and 3D case and has to be investigated in future works.

## 5. Application of SPH to Dust Collisions in PPDs, Conclusions, and Outlook

In this section we will present some preliminary applications of SPH simulations to dust collisions in protoplanetary disks. We will present two examples of previously unfeasible calculations of inter-particle collisions among macroscopic dust aggregates and will qualitatively compare them to similar dust experiments performed in the labora-

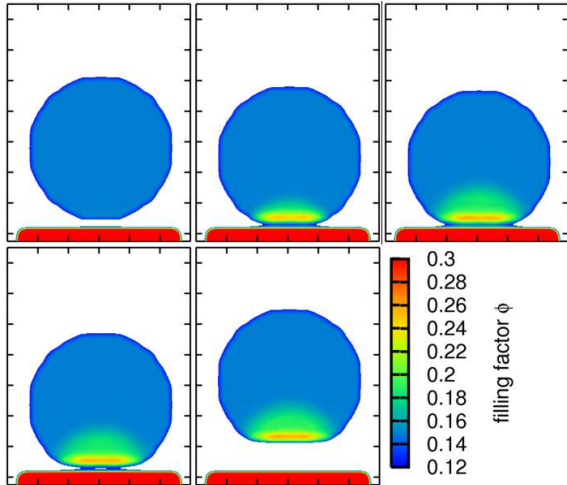


Fig. 19.— Sequence of snapshots of an SPH simulation of a fluffy dust aggregate with a radius of 0.5 mm, impacting a solid target at a velocity of  $0.2 \text{ m s}^{-1}$ . The time differences between subsequent images are 0.35 ms, 0.32 ms, 0.23 ms, and 4.45 ms, respectively. The colors denote different degrees of internal compaction. [See the electronic edition of the *Journal* for accompanying mpeg animations.]

tory. Then, we will speculate about how the SPH code should be used in research on protoplanetary growth. Finally we will sketch future work in preparation.

### 5.1. Qualitative comparison between SPH simulations and laboratory experiments

The strength of the SPH simulations – besides the well-known examples in hyper-velocity collisions – over laboratory experiments and molecular-dynamics simulations is that low-velocity collisions among arbitrary dust aggregates can be investigated. Here, we show two examples recently observed in the lab, which can so far not be described by any other model. Example 1 deals with the frequently-observed bouncing collisions in aggregate-aggregate interactions. Example 2 describes the impact of a single dust aggregate onto a solid flat target, which shows the co-occurrence of (partial) sticking *and* fragmentation.

#### 5.1.1. Example 1

Bouncing in collisions between dust aggregates has been observed in many laboratory experiments (Blum and Münch 1993; Langkowski et al. 2008, paper III; Heißelmann et al., in prep., will appear in this series), although molecular-dynamics simulations always show a direct transition from sticking to fragmentation when the collision energy exceeds a threshold value (Dominik and Tielens 1997; Wada et al. 2007, 2008). Nature obviously chooses a wider bouncing transition between those two stages, at least for aggregates above a certain size. It turns out that the SPH method is capable of describing the bouncing phase quite well. We have run a 3D SPH simulation of a low-velocity impact of a 1 mm (diameter) fluffy aggregate onto a flat target. Due to symmetry arguments, this is identical to a two-aggregate (central) collision with twice the collision velocity. In our case, the aggregate was composed of 33,377 SPH particles and had an initial volume filling factor of 0.15. All other material parameters were identical to those in the previous section, i.e.  $K_0 = 300 \text{ kPa}$ ,  $p_m = 1.3 \text{ kPa}$ ,  $Y = \sqrt{\Sigma|T|}$ . The impact velocity was  $0.2 \text{ m s}^{-1}$ , matching exactly the situation in the aggregate-wall experiments performed in paper III and also those in the aggregate-aggregate collisions investigated by Heißelmann et al. (in prep.) with a collision speed of  $0.4 \text{ m s}^{-1}$ . Fig. 19 shows a sequence of snapshots with a cut through the center of the aggregate, indicating the internal compaction due to the impact. Our simulation can correctly predict the coefficient of restitution of  $\sim 0.2$  (Blum and Münch 1993, Heißelmann et al., in prep.), although details in the compaction behavior still deviate from the laboratory results, which might be caused by insufficient resolution in the SPH simulation.

#### 5.1.2. Example 2

In the previous example, we have seen that bouncing marks the broad transition regime between sticking and fragmentation. However, in the case of the impact of a dust aggregate onto a solid target, laboratory experiments have shown that, for impact experiments above the fragmentation threshold, fragmentation is always accompanied by partial sticking of the aggregate to the target. This effect was first found by Wurm et al.

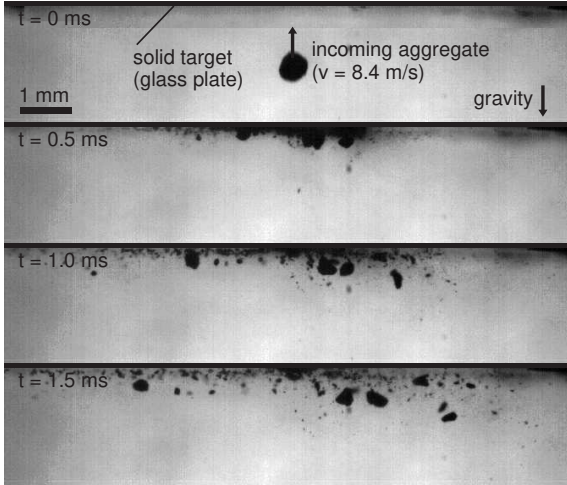


Fig. 20.— Image sequence of an experiment, in which a fluffy dust aggregate impacts a solid target at  $8.4 \text{ m s}^{-1}$ . Part of the aggregate sticks to the target after the collision. [See the electronic edition of the Journal for accompanying mpeg animations.]

(2005) for compacted dust aggregates and impact velocities above  $25 \text{ m s}^{-1}$  and later confirmed in our laboratory for  $\phi = 0.35$  aggregates and impact velocities above  $1 \text{ m s}^{-1}$ . Fig. 20 shows an image sequence of an impact experiment with fragmentation and partial sticking. An average of 10 % of the projectile mass sticks to an initially smooth target at normal impact, which is consistent with the low velocity results of Wurm et al. (2005). The remainder of the projectile mass is fragmented into a power-law mass distribution (see Blum and Münch 1993). The fragments leave the target under extremely flat angles. Our SPH simulation (Fig. 21, left) featuring the calibration parameters of Sect. 4.2 cannot reproduce the fragmentation behavior seen in the experiments. Here, the predominant part of the dust sample sticks to the target. Only a few bigger chunks and single SPH particles burst off. However, a simulation with the same setup, but using the shifted unidirectional compressive strength relation (Sect. 3.2) and a shear strength that is equal to the tensile strength, matches the experimental observations at least qualitatively (Fig. 21, right). From that we conclude that the SPH code is in principle capable of simulating fragmentation of highly-porous aggregates, even without the dam-

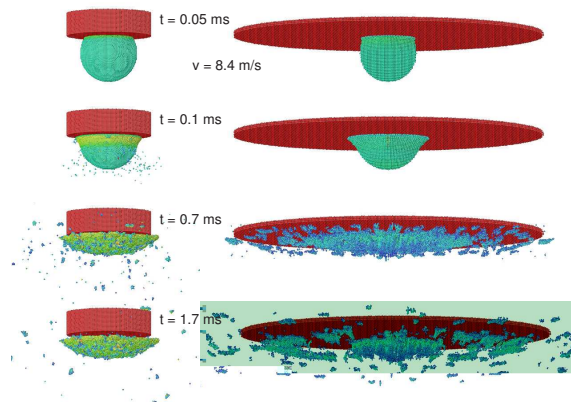


Fig. 21.— Image sequence of an SPH simulation, identical to the experiment shown in Fig. 20. The simulation with the calibrated parameters (**left**) cannot reproduce the experimental results, whereas a simulation using an unidirectional compression curve and  $\Sigma = |T|$  (**right**) can reproduce the qualitative findings of Fig. 20. [See the electronic edition of the Journal for accompanying mpeg animations.]

age model adopted in the original Sirono (2004) porosity model.

We conclude that the shear model  $Y = \Sigma^{0.5} \cdot |T|^{0.5}$  tested for the dynamic compression experiments (Sect. 4.1) is unable to explain the fragmentation findings which are rather dominated by shear and tension, whereas a shear model  $Y = \Sigma^0 \cdot |T|^1$  shows qualitative agreement. The imperfect shear model can also be responsible for the narrow but deep compressed volume in Fig. 16 compared to Fig. 9. A future task will therefore be to refine the shear calibration in a way that we will use  $Y = C \cdot \Sigma^\alpha \cdot |T|^{1-\alpha}$  with the free parameters  $C$  and  $\alpha$ . Comprising both experiments for calibration we will be able to find a shear model that can reproduce both cases.

## 5.2. Use of the SPH code in research on protoplanetary growth

The above examples show that the SPH method is a powerful tool to investigate the outcomes of protoplanetary dust collisions. When properly calibrated with laboratory experiments, SPH calculations allow access to parameter-space regions that are unavailable to laboratory experiments. Whereas molecular-dynamics simulations can be



used for studying collisions of very small dust aggregates, SPH is most useful for very large samples. Such samples, particularly those with fluffy compositions, cannot be built or treated in laboratories, and the experimental study of collisions seems impossible.

A particularly interesting and still unsolved problem is the dichotomy in the collision behavior of pairs of dust aggregates with similar and different sizes, respectively. In paper II we found sticking by deep penetration for impacts of mm-sized dusty projectiles into flat, cm-sized dusty targets (“projectile-target” collisions) above  $\sim 1 \text{ m s}^{-1}$ . Both dust aggregates, projectile and target, consisted of identical particles and had equal porosity. Using similar dust aggregates, but giving projectile and target comparable size (“projectile-projectile” collisions), Blum and Münch (1993) and Heißelmann et al. (in prep.) found that collisions either lead to bouncing or to fragmentation. Bouncing instead of sticking was also observed in paper II when the target aggregates were prepared such that the local radius of curvature corresponded to the projectile’s radius. To find out where the boundary between “projectile-target” and “projectile-projectile” collisions occurs, will be one of our future applications of our SPH code.

### 5.3. Future work

We have only begun to explore the potentials of SPH simulations of collisions between protoplanetary dust aggregates. Before we can start to investigate the full parameter space in protoplanetary dust collisions, i.e. before we can begin to find out what the collisional outcome is for all combinations of aggregate size, porosity, collision velocity, impact angle, state of rotation, temperature and state of sintering, material and size (distribution) of the constituent dust grains, etc., the material parameters of macroscopic dust aggregates have to be fully explored. This will be the next task in our investigation. To achieve this, we will perform more calibration experiments of the type described in this paper for dust aggregates of various compositions and porosities. In addition to that, other calibration experiments will be explored, like the ones described in Sects. 5.1.1 and 5.1.2.

### Acknowledgements

We thank M.-B. Kallenrode and the University of Osnabrück for providing access to the XRT setup and Jens Teiser for the first feasibility tests for the experiments. The SPH simulations were performed on the university and bwGrid clusters of the computing center (ZDV) of the University of Tübingen. This project was funded by the Deutsche Forschungsgemeinschaft within the Forschergruppe 759 “The Formation of Planets: The Critical First Growth Phase” under grants Bl 298/7-1, Bl 298/8-1, and Kl 650/8-1.

### REFERENCES

- Benz, W. and Asphaug, E. (1994). Impact simulations with fracture. I - Method and tests. *Icarus*, 107:98.
- Blum, J. (2004). Grain Growth and Coagulation. In Witt, A. N., Clayton, G. C., and Draine, B. T., editors, *Astrophysics of Dust*, volume 309 of *Astronomical Society of the Pacific Conference Series*, page 369.
- Blum, J. and Münch, M. (1993). Experimental investigations on aggregate-aggregate collisions in the early solar nebula. *Icarus*, 106:151.
- Blum, J. and Schräpler, R. (2004). Structure and Mechanical Properties of High-Porosity Macroscopic Agglomerates Formed by Random Ballistic Deposition. *Phys. Rev. Lett.*, 93(11):115503.
- Blum, J., Schräpler, R., Davidsson, B. J. R., and Trigo-Rodríguez, J. M. (2006). The Physics of Protoplanetary Dust Agglomerates. I. Mechanical Properties and Relations to Primitive Bodies in the Solar System. *ApJ*, 652:1768–1781.
- Blum, J. and Wurm, G. (2000). Experiments on Sticking, Restructuring, and Fragmentation of Preplanetary Dust Aggregates. *Icarus*, 143:138–146.
- Blum, J. and Wurm, G. (2008). The Growth Mechanisms of Macroscopic Bodies in Protoplanetary Disks. *ARA&A*, 46:21–56.
- Blum, J., Wurm, G., Kempf, S., Poppe, T., Klahr, H., Kozasa, T., Rott, M., Henning, T., Dorschner, J., Schräpler, R., Keller, H. U., Markiewicz, W. J., Mann, I., Gustafson, B. A., Giovane, F., Neuhaus, D., Fehchtig, H., Grün, E., Feuerbacher, B., Kochan, H., Ratke, L., El Goresy, A., Morfill, G., Weidenschilling, S. J., Schwehm, G., Metzler, K., and Ip, W.-H. (2000). Growth and Form of Planetary Seedlings: Results from a Microgravity Aggregation Experiment. *Phys. Rev. Lett.*, 85:2426–2429.
- Dominik, C. and Tielens, A. G. G. M. (1997). The Physics of Dust Coagulation and the Structure of Dust Aggregates in Space. *ApJ*, 480:647.
- Geretshausen, R. J., Speith, R., Güttler, C., Krause, M., and Blum, J. (2009). Numerical Simulations of Highly Porous Dust Aggregates in the Low-Velocity Collision Regime. *A&A*. in prep.

- Hayashi, C., Nakazawa, K., and Nakagawa, Y. (1985). Formation of the solar system. In Black, D. C. and Matthews, M. S., editors, *Protostars and Planets II*, pages 1100–1153.
- Heim, L.-O., Blum, J., Preuss, M., and Butt, H.-J. (1999). Adhesion and Friction Forces between Spherical Micrometer-Sized Particles. *Phys. Rev. Lett.*, 83:3328–3331.
- Krause, M. and Blum, J. (2004). Growth and Form of Planetary Seedlings: Results from a Sounding Rocket Microgravity Aggregation Experiment. *Phys. Rev. Lett.*, 93(2):021103.
- Langkowski, D., Teiser, J., and Blum, J. (2008). The Physics of Protoplanetary Dust Agglomerates. II. Low-Velocity Collision Properties. *ApJ*, 675:764–776.
- Libersky, L. D., Petschek, A. G., Carney, T. C., Hipp, J. R., and Allahdadi, F. A. (1993). High strain lagrangian hydrodynamics: A three-dimensional sph code for dynamic material response. *Journal of Computational Physics*, 109(1):67 – 75.
- Melosh, H. J. (1989). *Impact cratering: A geologic process*.
- Monaghan, J. J. (2005). Smoothed particle hydrodynamics. *Reports of Progress in Physics*, 68:1703–1759.
- Monaghan, J. J. and Gingold, R. A. (1983). Shock simulations by the particle method sph. *Journal of Computational Physics*, 52:374.
- Paszun, D. and Dominik, C. (2008). Numerical determination of the material properties of porous dust cakes. *A&A*, 484:859–868.
- Randles, P. W. and Libersky, L. D. (1996). Smoothed particle hydrodynamics: Some recent improvements and applications. *Computer Methods in Applied Mechanics and Engineering*, 139(1-4):375 – 408.
- Sirono, S.-I. (2004). Conditions for collisional growth of a grain aggregate. *Icarus*, 167:431–452.
- Teiser, J. and Wurm, G. (2009). High-velocity dust collisions: forming planetesimals in a fragmentation cascade with final accretion. *MNRAS*, 393:1584–1594.
- Torquato, S., Truskett, T. M., and Debenedetti, P. G. (2000). Is Random Close Packing of Spheres Well Defined? *Phys. Rev. Lett.*, 84:2064–2067.
- Wada, K., Tanaka, H., Suyama, T., Kimura, H., and Yamamoto, T. (2007). Numerical Simulation of Dust Aggregate Collisions. I. Compression and Disruption of Two-Dimensional Aggregates. *ApJ*, 661:320–333.
- Wada, K., Tanaka, H., Suyama, T., Kimura, H., and Yamamoto, T. (2008). Numerical Simulation of Dust Aggregate Collisions. II. Compression and Disruption of Three-Dimensional Aggregates in Head-on Collisions. *ApJ*, 677:1296–1308.
- Weidenschilling, S. J. (1977a). Aerodynamics of solid bodies in the solar nebula. *MNRAS*, 180:57–70.
- Weidenschilling, S. J. (1977b). The distribution of mass in the planetary system and solar nebula. *Ap&SS*, 51:153–158.
- Weidenschilling, S. J. and Cuzzi, J. N. (1993). Formation of planetesimals in the solar nebula. In Levy, E. H. and Lunine, J. I., editors, *Protostars and Planets III*, pages 1031–1060.
- Weidling, R., Güttler, C., Blum, J., and Brauer, F. (2009). The Physics of Protoplanetary Dust Agglomerates. III. Compaction in Multiple Collisions. *ApJ*, 696:2036–2043.
- Wurm, G., Blum, J., and Colwell, J. E. (2001). NOTE: A New Mechanism Relevant to the Formation of Planetesimals in the Solar Nebula. *Icarus*, 151:318–321.
- Wurm, G., Paraskov, G., and Krauss, O. (2005). Growth of planetesimals by impacts at  $\sim 25$  m/s. *Icarus*, 178:253–263.

---

This 2-column preprint was prepared with the AAS L<sup>A</sup>T<sub>E</sub>X macros v5.2.